PAPER • **OPEN ACCESS**

Toward detailed modeling of tires with linear elastic rubber compounds using finite element method

To cite this article: Baurice Sylvain Sadjiep Tchuigwa *et al* 2024 *IOP Conf. Ser.: Earth Environ. Sci.* **1380** 012018

Toward detailed modeling of tires with linear elastic rubber compounds using finite element method

Baurice Sylvain Sadjiep Tchuigwa[1*], Jan Krmela[1, 2] and Jan Pokorny[1]

[1] Department of Transport Means and Diagnostics, Faculty of Transport Engineering, University of Pardubice, Studentská 95, 532 10 Pardubice, Czech Republic
[2] Faculty of Industrial Technologies in Púchov, Alexander Dubček University of Trenčín, Ivana Krasku 491/30, 02001 Púchov, Slovak Republic

[*]E-mail: bauricesylvain.sadjieptchuigwa@student.upce.cz, sylvainsadjiep@gmail.com , jan.krmela@tnuni.sk

Abstract. Against a backdrop of increasing depletion of natural and energy resources and worsening global warming, the tire industry, like many other industries, is currently confronted with the pressing need to enhance not only its resilience but also the sustainability and cost-effectiveness of its products through advanced numerical simulations. Numerical simulation is a valuable tool in the tire development process that provides manufacturers with in-depth insights into their products from design to mass production. This paper aims to introduce a detailed finite element-based modeling process for tires that can be used for a wide range of simulations, including steady state, transient rolling, and failure scenarios such as layer delamination, blowout, and part breakage. The selected tire for the implementation in this study is designated 175/75R14 and was modeled in a static loading setup in ABAQUS standard with an implicit scheme considering linear elastic rubber compounds and other assumptions. Unlike the commonly used homogenized approach for reinforced layers, the proposed method takes into account the real physical and mechanical properties of the tire structure. In addition, important information pertaining to the creation of mesh and the interactions between elements is provided. The obtained results align with the assumptions and can serve as a proof of concept for more detailed and advanced tire modeling and enhancement in the future.

1. Introduction

One study that formed the basis for finite element-based tire modeling with a linear elastic material model can be traced back to the early 1970s, during which researchers and engineers such as Ridha[1] and Zorowski[2] started to develop a comprehensive FEA (Finite Element Analysis) framework to simulate the static response of tires under different loading conditions. Utilizing a linear elastic material model, they laid the groundwork for subsequent research in tire development. This breakthrough inspired many researchers, such as Noor[3], who introduced two shell-based nonlinear tire strategies, in axisymmetric and 3D, with contact constraints enforced using the perturbed Lagrange approach. This strategy showed satisfying results in predicting the mechanical and thermal response in tire-pavement interaction with friction. Similarly, Davis[4]compared the performance of bias-ply and radial tires under varying loads, highlighting the importance of tire construction in determining structural response.

Given that tires are made of some reinforced layers, their modeling is very complex. Thus, several methods have been proposed in the literature to model reinforced layers in tires. Krmela et al.[5] proposed an orthotropic material based on the modeling of the tires with linear elastic

materials exploiting composite finite elements. Li et al. [6] investigated the effect of tire construction parameters on static response using FEA with a linear elastic material model. Specifically, the authors examined the impact of construction parameters on tire deformation and stress distribution by systematically altering parameters such as ply orientation and cord stiffness. Their results provided valuable insights into the optimization of tire construction design for improved static performance. Furthermore, computational techniques have progressed, allowing researchers to increase the accuracy and efficiency of finite element-based tire modeling. Wang et al. [7] adopted the same composite approach to simulate tire rolling steady-state using arbitrary Lagrange Eulerian formulation (ALE). Wang et al. [8] instead adopted a linear elastic composite model and validated its performance with experimental tests. The main drawback associated with the laminar approach is that it is difficult to model and predict the failure mechanism[9], [10] of the matrix, the rebar, or the cohesive bond connecting them. Therefore, detailed modeling with real rebars not only allows us to get the previously known results but also opens the doors to failure modeling. Moreover, with the ABAQUS[11] embedded constraint type, this can be achieved without the need to densify the mesh in the vicinity of incorporated reinforcements.

In this paper, we present a succinct modeling of the static loading of a selected tire at a high loading rate in ABAQUS using the dynamic implicit solver assuming the following:

- All materials are considered linear elastic and defined by their E and ν;
- Rubber compounds are uniform and, hence, have the same mechanical properties;
- The rim is modeled as a rigid body using coupling contact;
- The whole bead model is adopted[12];
- The rigid road model is considered;

2. Description of the numerical model

2.1 Dimensions

We consider the tire structure with the designation 175/75R14[13] as a specimen for this study.

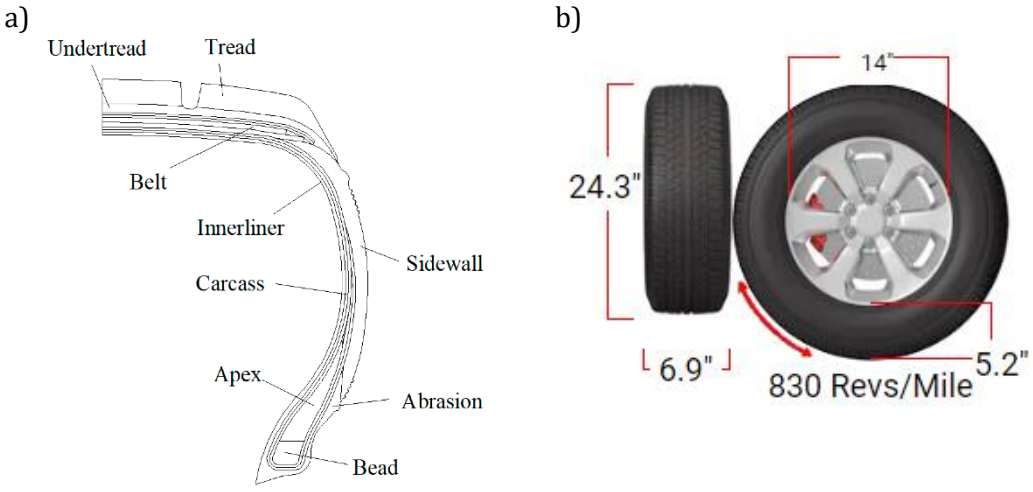

Figure 1: view and part of the 175/75R14 tire[16]

Its half cross-section is shown in Fig. 1a and with dimensions: 24.3" (618 mm) diameter, 6.9" (175

mm) tread width, 14" (355.6 mm) wheel diameter, 5.2" (131 mm) sidewall, 76.3" (1940.5 mm) circumference depicted in Fig. 1b.

2.2 Creation of tire parts

Carcass: Though we did not get enough information on the circumferential distribution of this element from the tire manufacturer, we defined them as considered a set of 300 carcass crowns with shape in Fig. 2 and distributed uniformly around a 360-degree revolution angle with respect to the transversal direction. To ease the computation, we defined them as 1D elements (called wire in ABAQUS) and assigned a beam-type behavior. The advantage of such a simplification is that it avoids ending up with a denser mesh at this element, which would result in a smaller stable time increment, a downfall for the solution method with an explicit solver. As for their section, reinforcements are circular with a diameter $\emptyset_{carcass} = 1\ mm$. These beam elements have six degrees of freedom at each node: three translations (1–3) and three rotational (4–6).

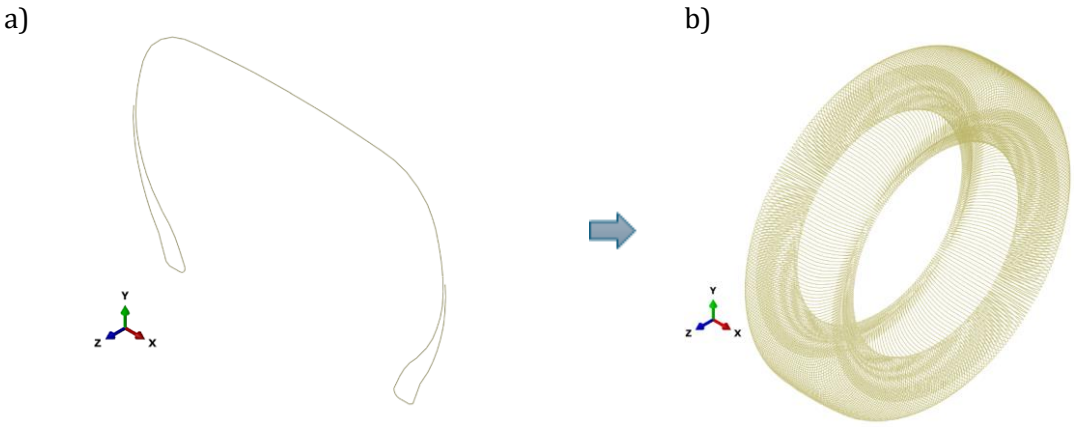

Figure 2: tire carcass creation process. a) a single element. b) set of 300 carcass

Textile cords: There is only one layer of textile cords (see Fig. 3) and they are embedded in the layer beneath the undertread (see Fig. 1.a). Similarly, as carcass elements, they are also defined as

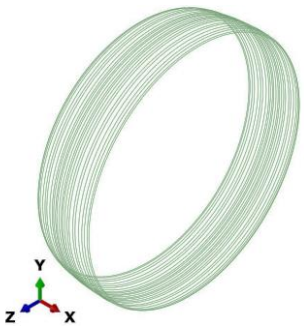

Figure 3: tire textile cords creation.

1D elements with a beam-type behavior and circular section of $\emptyset_{textile} = 0.8mm$.

Steel cords: There are two layers (see Fig. 4) embedded in the rubber layers above the carcass host layer (see Fig. 1.a). Similarly, as carcass elements, we defined them as 1D elements with a beam-type behavior. Each of the cords is of diameter $\emptyset_{steel} = 0.6mm$, and they are spread following the middle line of the two thin layers shown in Fig. 1.a

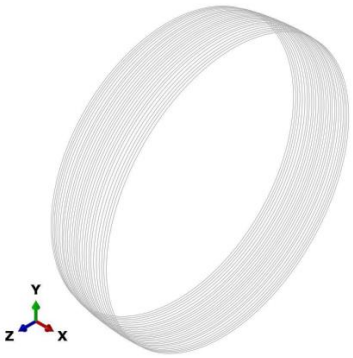

Figure 4: tire steel cords creation.

Rubber compounds: following the above assumption, the resulting rubber area is shown in Fig. 5.

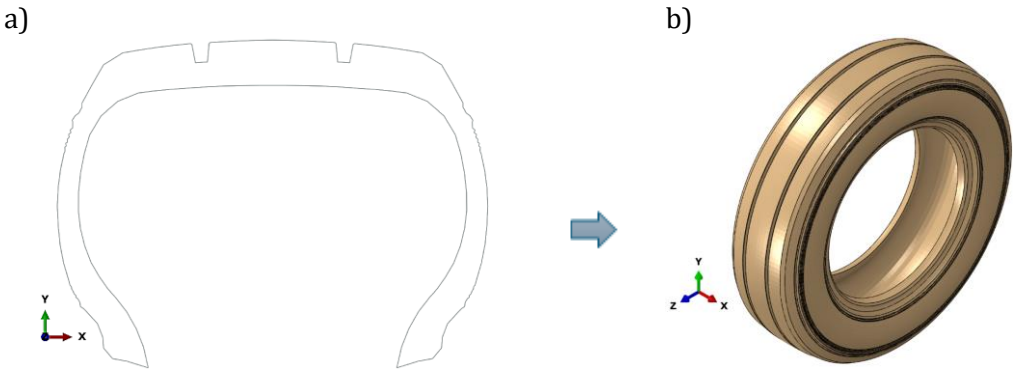

Figure 5: tire rubber compound creation. a) cross-section, b) rubber 3D model

Bead: this part was modeled as solid (3D entity) with its assumed whole section highlighted in Fig. 6.

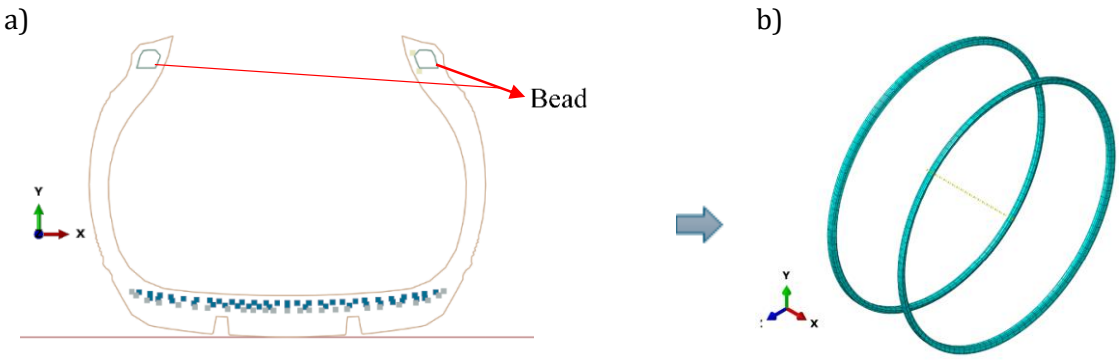

Figure 6: tire bead creation. a) cross-section, b) rubber 3D model

Road: we modeled the ground as a rigid flat surface of dimensions 800x1200mm^2, see Fig.7.

Figure 7: top view on the rigid road.

Note: In the modeling capabilities of ABAQUS, embedded constraints are employed to incorporate the abovementioned reinforcements (steel cords, carcass, textile cords and bead) in their host matrix. In the backend, the Program automatically deducts the area of these reinforcements from that of the hosting matrix.

2.3 Material properties

Material properties adopted for the different parts of the tire are reported in Table 1. For the sake of simplicity, we assumed that rubber compounds have the same mechanical properties.

Table 1. tire component mechanical properties

Parts	Density(ρ) [Kg/m3]	Young's modulus (E) [MPa]	Poisson's ratio (ν)
Rubber compounds	1200	100	0.485
Bead	7850	164 600	0.30
Textile cords	1250	1250	0.30
Carcass	1250	1900	0.40
Textile cord	1250	1900	0.35
Steel cords	7850	210 000	0.30

2.4 Mesh properties:

In order to avoid unnecessary mesh densification in the vicinity of the reinforcing bars, we meshed each tire element separately. Then in the next section, we describe how to link them through the interaction features. Table 2 shows the type of mesh chosen for each of the parts created above. Table 2 presents the mesh type chosen for each of the above-created parts.

Table 2. Properties of the mesh

Parts	Element	Element type	View
Rubber compounds	3D solid	C3D8RH: 8-node linear brick, reduced integration with hourglass control.	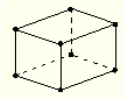
Bead	3D solid	C3D8RH: 8-node linear brick, reduced integration with hourglass control	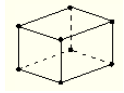
Textile cords	3D beam	B32H: 3-node quadratic hybrid elements	
Carcass	3D beam	B32H: 3-node quadratic hybrid elements	
Steel cords	3D beam	B32H: 3-node quadratic hybrid elements	
Road	3D Shell	S4R: 4-node linear shell with hourglass control	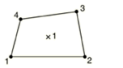

Where the letters R and H, respectively, stand for reduced integration with hourglass control and hybrid

Reduced integration is a remedy to the issue of shear locking caused by full integration. However, its implementation is associated with a hourglass shortcoming, which materializes with zero-strain energy mode, leading to element distortion. Thus, it is used together with hourglass control to circumvent this instability. Besides this, hybrid formulation or mixed variational formulation (u-p), is employed to alleviate volumetric locking observed in nearly or fully incompressible materials, characterized by $\nu \in [0.475, 0.499]$. Further details about this formulation can be found in ABAQUS documentation.

More rigorously, second-order elements are often recommended to be utilized in the tread zone close to the ground to ensure proper contact pressure transmission to the ground, as extensively studied in computational mechanics materials [14], [15]. However, we consider linear elements for simplicity and mesh the structure so that the slave body's elements are smaller than the master body's elements. The above-created parts were meshed as depicted in Fig. 8.

Figure 8: meshed model

2.5 Boundary conditions

Before all, we define an interaction property under the '*interaction*' menu, where we set normal and tangential contact properties. Here, we assumed a friction coefficient $\mu_s = 0.5$, and under the

normal contact option, we adopted the *hard contact* approach because it is the closest behavior to reality as it allows no penetration, as illustrated in Fig. 9.

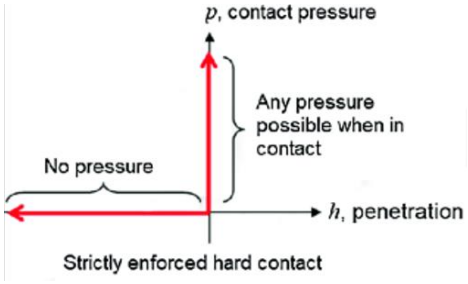

Figure 9: Hard contact law[17]

As for the contact enforcement theory, we chose the penalty method for tangential contact and let the computer select the best contact enforcement approach for the normal contact among those available (penalty, augmented Lagrange, and direct method). Substantial details about computational mechanics theory sustaining these approaches can be found in [14], [15]

- *Rim-tire interaction*: Given that forces from the vehicle are transmitted to tires through the rim and knowing that the latter is much stiffer than the former, we assume the rim is a rigid body (non-deformable). In ABAQUS, this is achieved by linking the rim's center (*reference point*) to its contact zone with the tire through *coupling constraint*. To ensure coherence with the concept of a rigid rim, we activated *kinematic coupling* under the coupling window and ticked on all the degrees of freedom. This constraint is compatible with this loading as the rim does not restrict the tire from deforming vertically. However, the rim's humps restrict any lateral slip of the tire as the inflation pressure traps it to remain in the hump. For other load scenarios, such as cornering, braking, etc., the same constraint remains valid as long as the rigid rim assumption holds;
- *Road-tire interaction:* This boundary condition is enforced by defining a *general contact* interaction with properties indicated in the Contact setting. By selecting this interaction, the *Program automatically controls the self-contact constraint*. This condition helps prevent violation of contact in the body with itself;
- Rubber part-carcass embedded constraint: under the interaction menu, we selected the rubber as the host region and carcass as embedded elements;
- Similarly to rubber-carcass embedded constraint, those of steel cords, textile cords and beads were also treated the same way.

Note: Enforcing embedded constraints leads to a much faster computation as it helps eliminate unnecessary contact checks. Another idea to work it around would be to typically define these elements and link them with tied contact with rubber compounds. However, the reserve side of such a choice would be the small size of the element in the vicinity, leading to an increase in mesh size and long execution time.

2.6 Solver settings:

We start by recalling the discretized equation of motion derived from the weak form of linear momentum associated with this problem. The differential equation reads as

$$M\ddot{u} + C\dot{u} + Ku = F_{ext}(t) - F_{contact} \quad (1)$$

Where M, C, K, F_{ext} and $F_{contact}$ are the mass matrix, damping matrix, stiffness matrix, vector of external forces, and contact force, respectively. We precise that $M, C,$ and $K \in \mathcal{M}^{n\times n}$: the space of square matrix of order n and $F_{ext}, F_{contact} \in \mathbb{R}^n$: the vector space of order n.

Since we have considered no strain rate-dependent source $C = 0$, so we end up with the the following equation

$$M\ddot{u} + Ku = F_{ext}(t) - F_{contact} \quad (2)$$

To this equation, we add the contact condition. When the kinetic energy becomes important, the inertial dynamic-induced effect outweighs the purely static consideration. While the static solver is suitable for most static and dynamic problems where the excitation frequency is less than a third of the problem's natural frequency, dynamic solvers are suitable for dynamic problems with frequencies of any order. ABAQUS hosts two solvers for solving dynamic problems: implicit and explicit solvers. While the explicit solver solves for acceleration and then derives velocity and displacement from the numerical scheme, the implicit solver does the opposite. This implies that the latter must combine a spatial solution scheme (Newton Raphson) and a temporal scheme (Newmark, etc.) to solve the equation for a given time interval. The advantage is that a large time step can be chosen, while the main disadvantage is that it requires more memory and can be computationally expensive. As for the explicit solver, its main advantages are its memory efficiency and computational rapidity; however, it is conditionally stable because of its stability dependence on tiny time steps. For the current study, we chose the dynamic implicit solver with default setting except for the number of attempts I_A , which we increased to 5. A single simulation step of 1s was considered.

2.7 Load definition

Three loads were considered: vertical load F_y, gravity and the inflation pressure p_{in}.

Vertical load: it represents the portion of the vehicle's load transmitted to the wheel via the rim. This force was applied at the reference point (RP1) defined at the rim's center. We assumed a linear dependence on the time, as depicted in Fig. 10.

a) b)

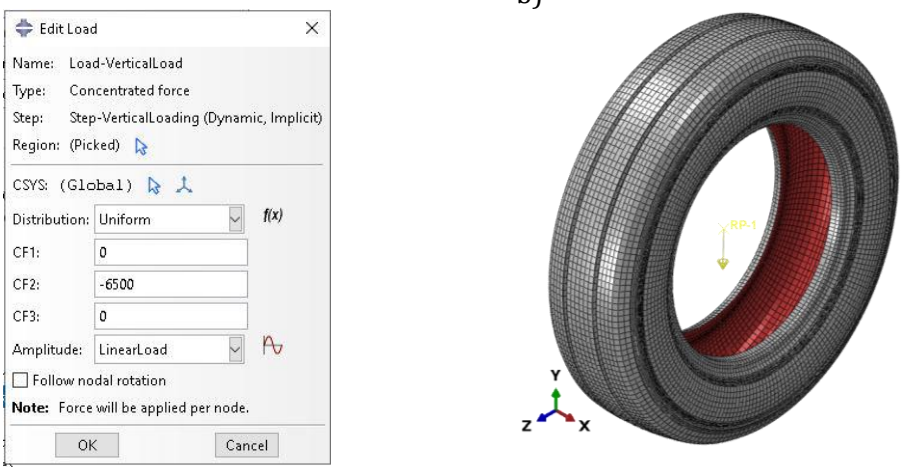

Figure 10: Vertical load definition from the reference point RP1

Gravity load: We have included the effect of gravity for more realistic results by defining it as a supplementary load.

Inflation pressure: an inward normal pressure of 0.25MPa was applied on the inner surface of the rubber (called inner liner) as illustrated in Fig. 11.

a) b)

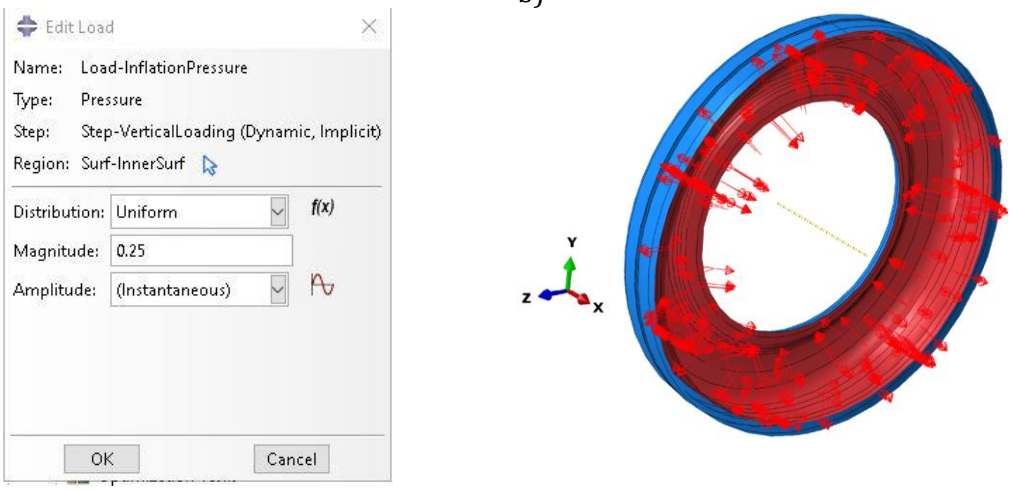

Figure 11: Inflation pressure definition

3. Results and discussion:

Given that the analysis took too much time (more than 8 hours), considering that the model was computationally stable and that material behaviors were considered linear elastic, a linear tendency in the results was reached after 0.045s. So, we terminated the simulation at 0.071s after 38 successful time increments. Hereafter, we report a few of the key results obtained.

3.1 Vertical displacement Uy *in mm (see Fig. 12)*:

a) At $t = 2.6781 \times 10^{-2}$s b) At $t = 4.2222 \times 10^{-2}$s

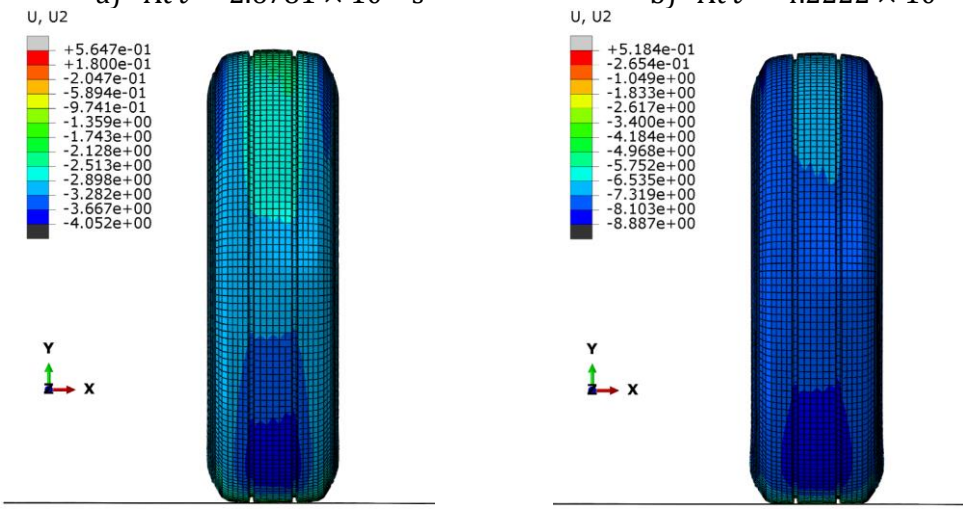

Figure 12 (part one): evolution of the vertical deformation U_y in the lower section of the tire over the time

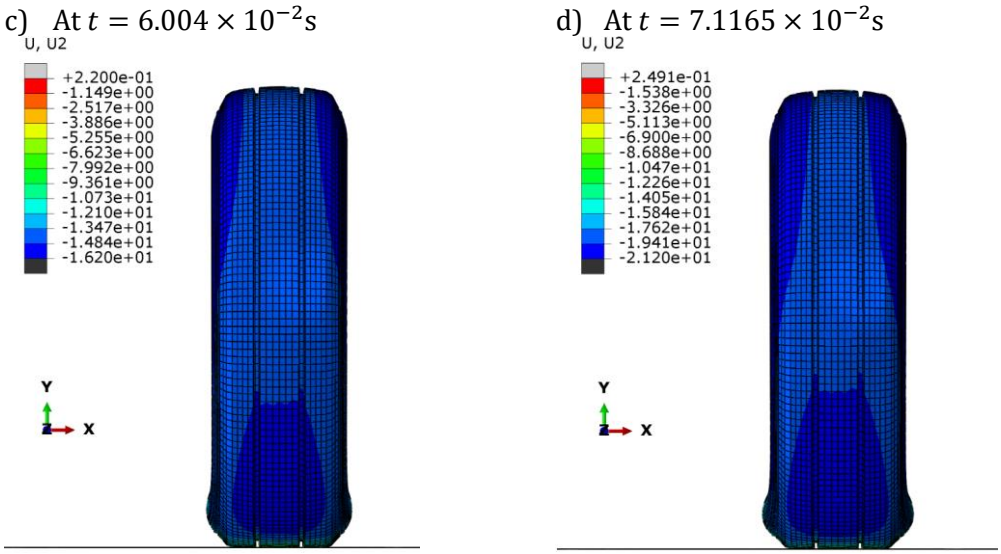

Figure 12(part two): evolution of the vertical deformation U_y in the lower section of the tire

3.2 Transversal displacement U_x in mm:

When the applied load increases, the deformation U_x of the tire at the bottom portion along x-axis rises too, as shown in the bottom cross-section in Fig. 13.

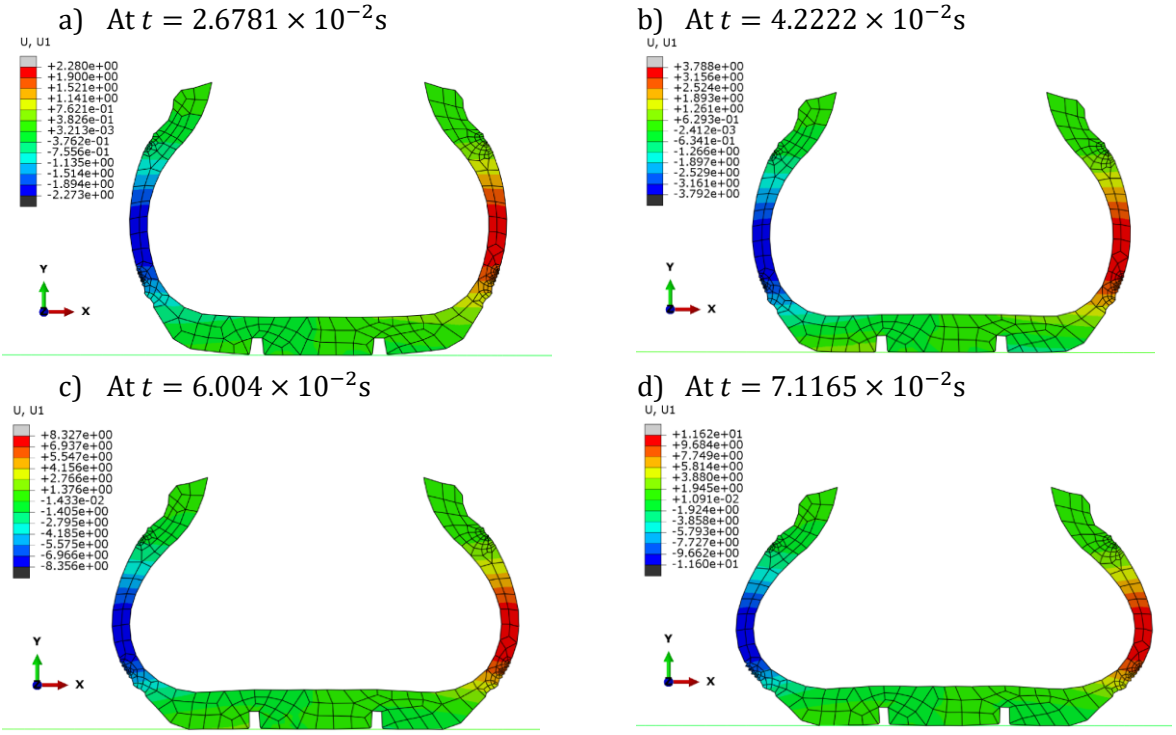

Figure 13: evolution of the transversal deformation in the lower section of the tire over the time

At each time step, we can note in Fig. 13 that the error between U_x at the left and right crown is less than 1.5%, a result that is physically logical given the symmetry of the tire, the intervening loads, and the isotropy of the behavior of the materials considered. With regard to the

effectiveness of the model's contact behavior, it is worth mentioning that there is no penetration. This is in line with the defined contact boundary conditions.

3.3 Von Mises stress in MPa:

Recalling that Von Mises stress is given by the formula

$$\sigma_{VM}(t) = \sqrt{\frac{3}{2}\sigma_{dev}(t) : \sigma_{dev}(t)} \tag{3}$$

Where $\sigma_{dev} = \sigma_{vol} - \sigma$ and $\sigma_{vol} = \frac{1}{3}tr(\sigma)I$ are the deviatoric and hydrostatic components of Cauchy stress, respectively. The distribution of σ_{VM} in the structure over the time is shown in Fig. 14.

a) At $t = 2.6781 \times 10^{-2}$s

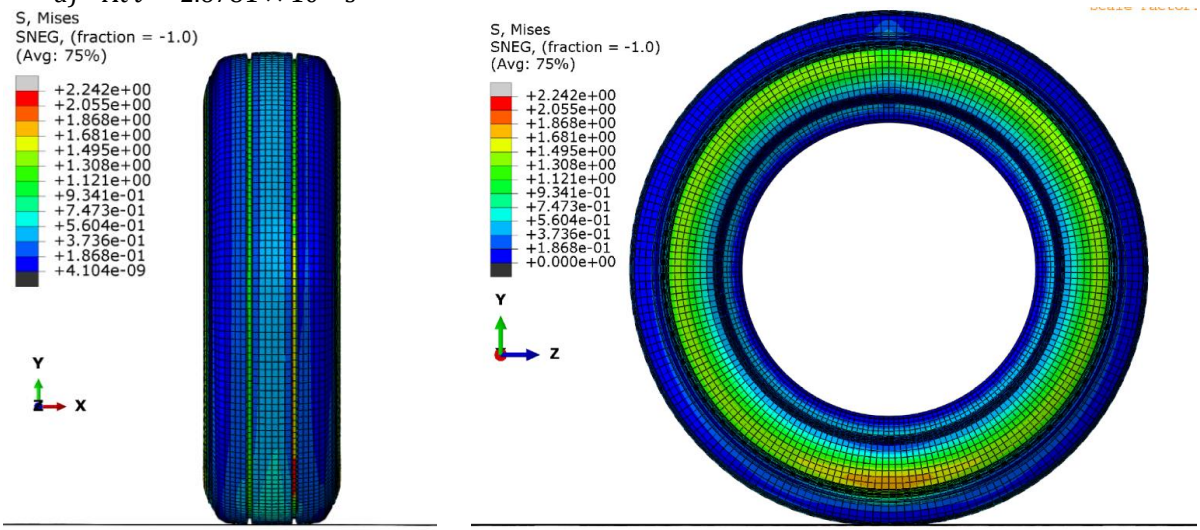

b) At $t = 4.2222 \times 10^{-2}$s

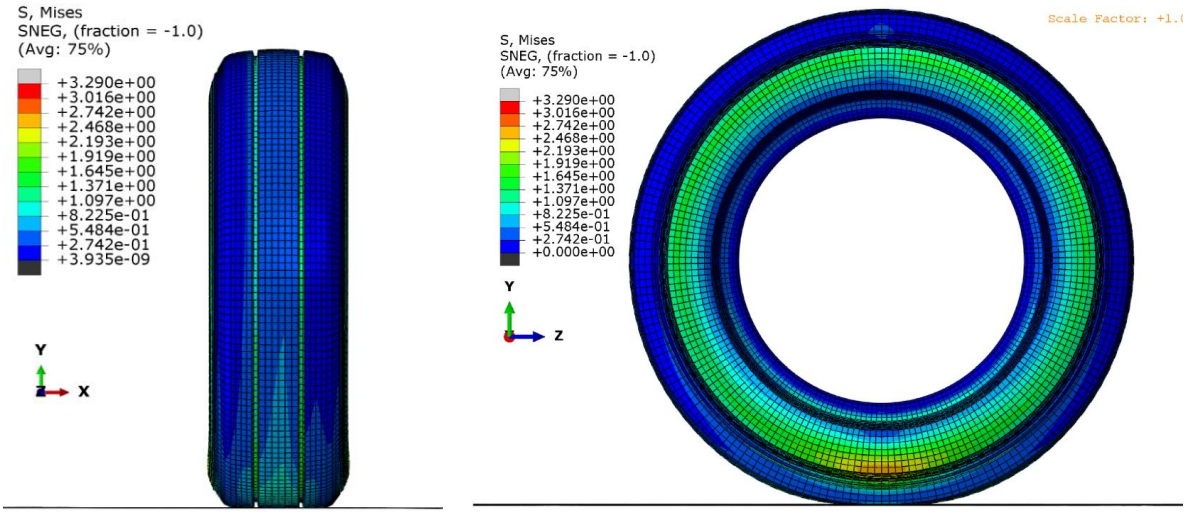

Figure 14(part one): evolution of Von Mises stress in the tire over the time

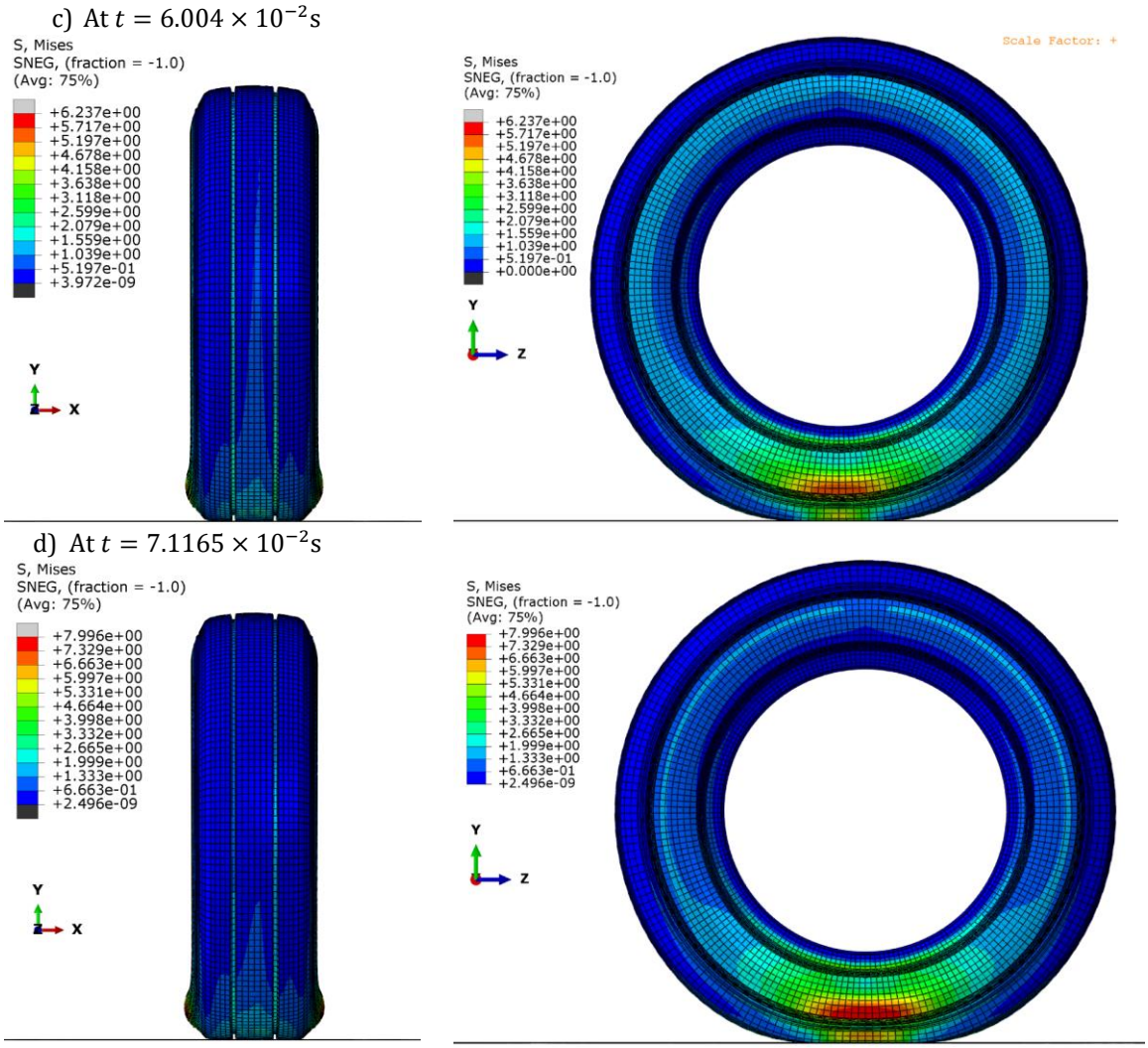

Figure 14(part two): evolution of Von Mises stress in the tire over the time

In line with the tire's known failure zone in the static experimental tests[9], [10], we observed a densification of stresses in the sidewall region at the right of the contact zone caused by the lateral deformation associated with the radial deformation.

3.4 Contact pressure distribution

As the vertical load increases, the amplitude, distribution, and area of the contact patch change, as succinctly shown in Fig. 15

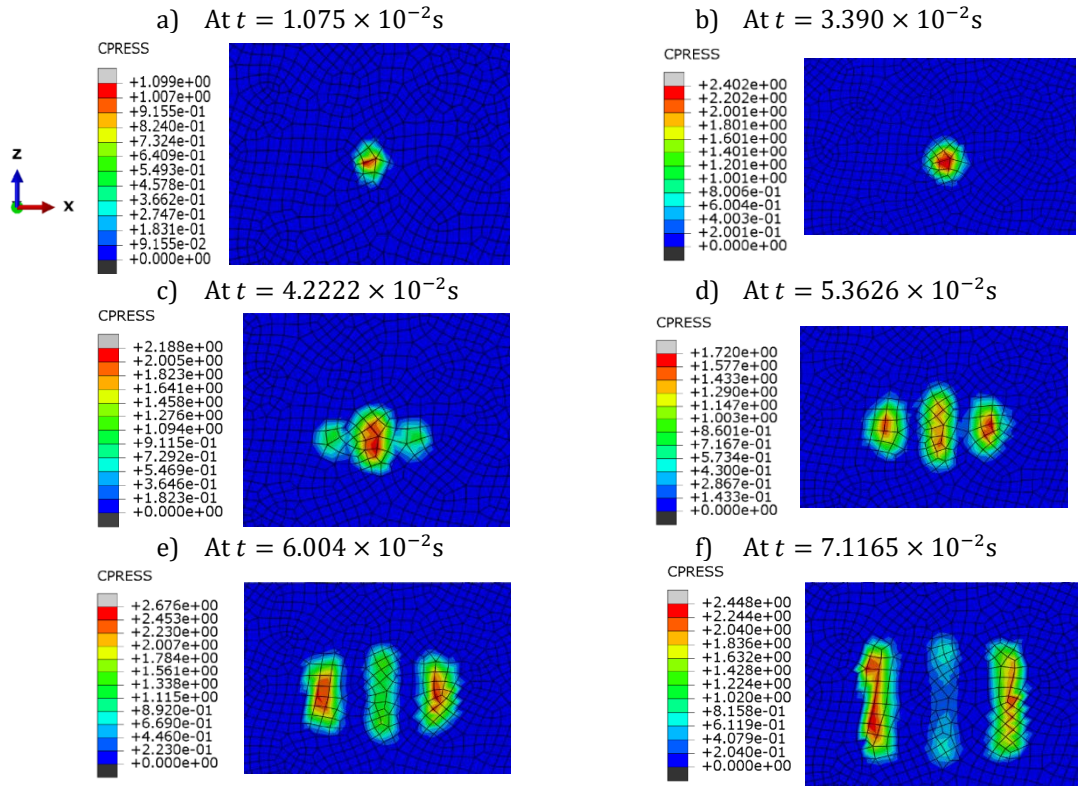

Figure 15: evolution of the contact pressure and shape within the time

3.5 Bead:

The maximum σ_{VM} stress in bead part at 7.10×10^{-2}s is 82.21MPa, as shown in Fig. 16

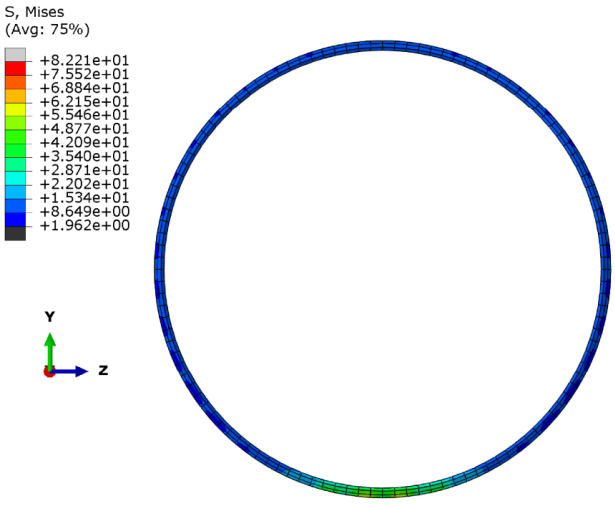

Figure 16: Stress distribution in the bead at 7.1165×10^{-2}s.

Here, we note that the lower part is the most solicited, as we also observed in rubber compounds.

3.6 Steel cords:

The visualization of the stress distribution in steel cords reveals a high level of solicitation more accentuated on cords in the bottom layer, as shown in Fig. 17.

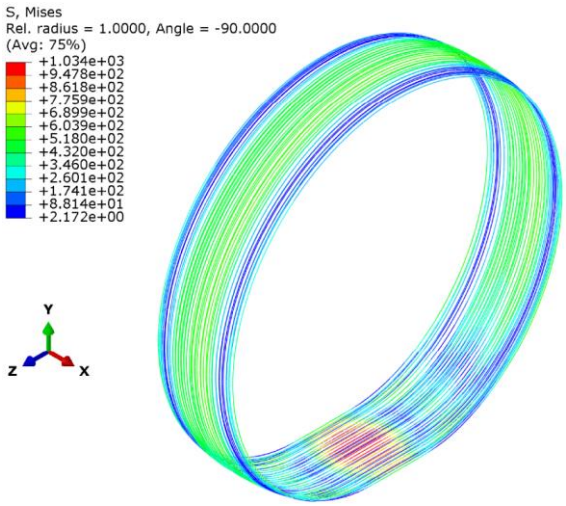

Figure 17: Stress distribution in steel cords at 7.1165×10^{-2}s.

3.7 Textile cords

Fig. 18 presents stress distribution in textile cords.

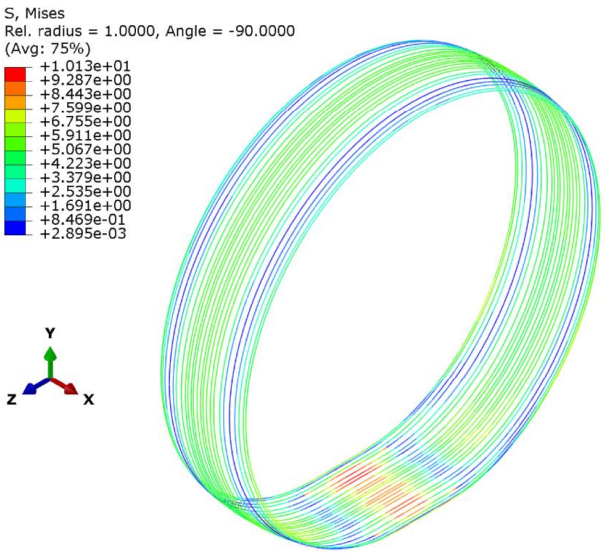

Figure 18: Stress distribution in textile cords at 7.1165×10^{-2}s.

3.8 Carcass:

Fig. 19 depicts the distribution of stress in all the carcasses of the model, and we observe that the zone most solicited in the carcass is located in the lower part in contact with the road.

a) All carcass

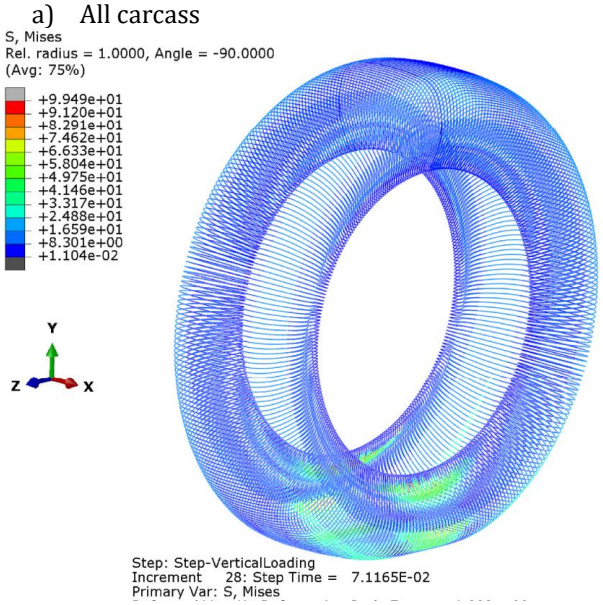

b) On an arbitrarily selected carcass

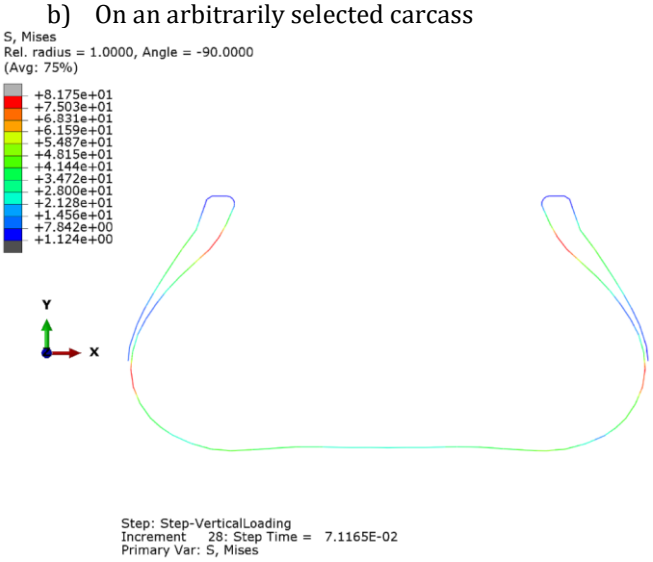

Figure 19: Stress distribution in carcass

3.9 Analysis of the results:

In this section, we focus on a more in-depth analysis of the results at two particular points and the ground contact zone as follows.

- Point A: where the maximum vertical displacement $|U_y|$ is obtained;
- Point B: where the maximum value of σ_{VM} is observed;
- The distribution of contact pressure along the transversal direction through the center of the contact patch.

Point A: where the maximum vertical displacement $|U_y|$ is obtained

At this point, we have extracted the values of the vertical displacement and applied force at each of the computed time steps. Using ABAQUS built-in functionality, we located this point in the lower portion of the tire and precisely on the tread outermost surface, as shown in Fig. 20

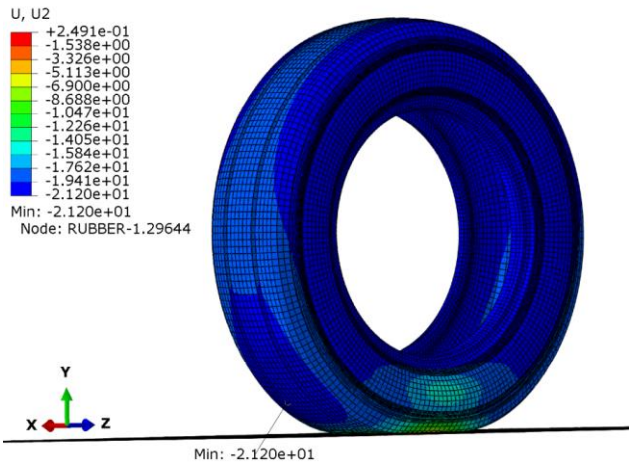

Figure 20: Location of the point with $max|U_y|$

The retrieved data are reported in Table 3

Table 3: values of F_y , $|U_y|$ and σ_{VM} over the time

Time (s)	F_y (N)	$\|U_y\|$ (mm)	σ_{VM} (MPa)
0	0	0	0
0.011	69.875	1.18	0.289
0.027	174.078	3.99	0.331
0.034	220.353	6.02	0.370
0.042	274.445	8.84	0.436
0.054	348.568	13.40	0.571
0.060	390.261	16.20	0.676
0.071	462.575	21.20	0.907

The loading sequence defined as the applied force F_y versus the time, is linear as depicted in Fig. 21.a. The selected corresponding response $|U_y|$ and σ_{VM} are also shown with respect to time in Fig. 21.b

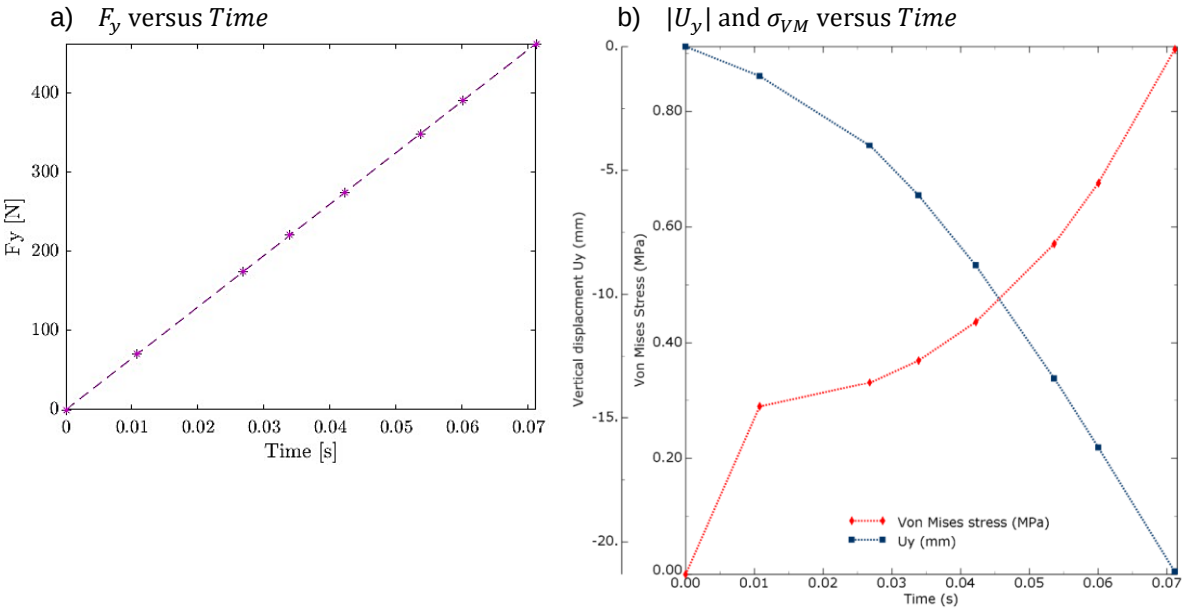

Figure 21: dependence of F_y, $|U_y|$ and σ_{VM} versus Time

More generally, for practical validation with experimental data collected during the laboratory testing of the selected tire, it is better to plot the relationship between F_y and $|U_y|$ (see Fig. 22)

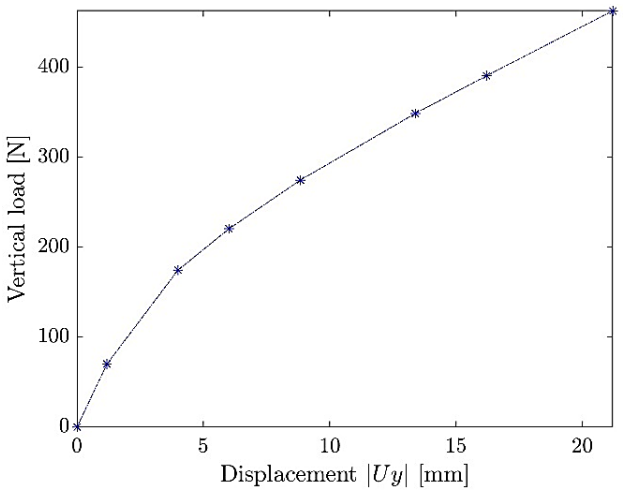

Figure 22: dependence of F_y versus $|U_y|$

Indeed, during the vertical motionless test of the tire, the controlled parameter is the applied force Fy, and the measured parameter is the vertical displacement $|U_y|$. So, at this point, once $|U_y|_{\text{experiment}}$ is recorded, it is possible to carry out the first validation of the proposed model. With the set of data ($|U_y|$, F_y) at hand, it is straightforward to compute the vertical stiffness of the tire using the formula

$$k_y = \frac{\partial F_y}{\partial U_y} \tag{4}$$

Furthermore, we can also assess the evolution of Von Mises stress as a function of $|U_y|$ at the same point as plotted in Fig. 23. Beyond the fourth point in this figure, we can assume a linear dependence between σ_{VM} and $|U_y|$, which is in total agreement with material assumptions.

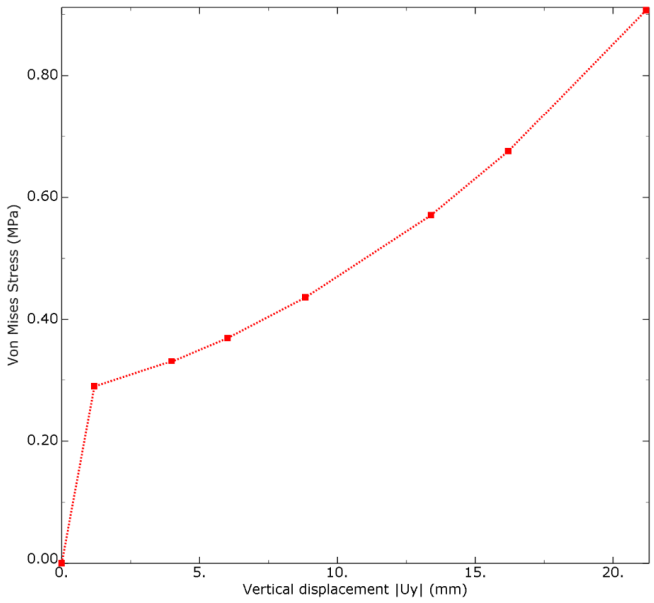

Figure 23: dependence of σ_{VM} versus $|U_y|$

Point B: where the maximum value of σ_{VM} is observed

Using a cross-section with a plane xy passing through the center of the rim, it is easier to visualize the location of the point B, as shown in Fig. 24.

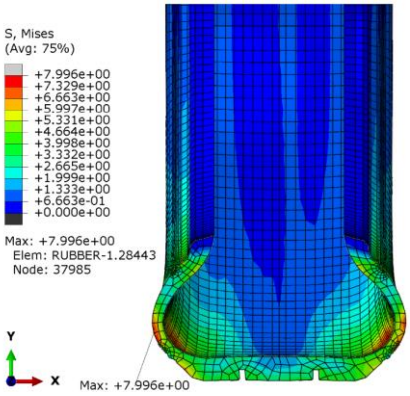

Figure 24: location of the point with maximum σ_{VM}

Fig. 25 depicts the dependence of U_x, U_y and σ_{VM} as a function of time.

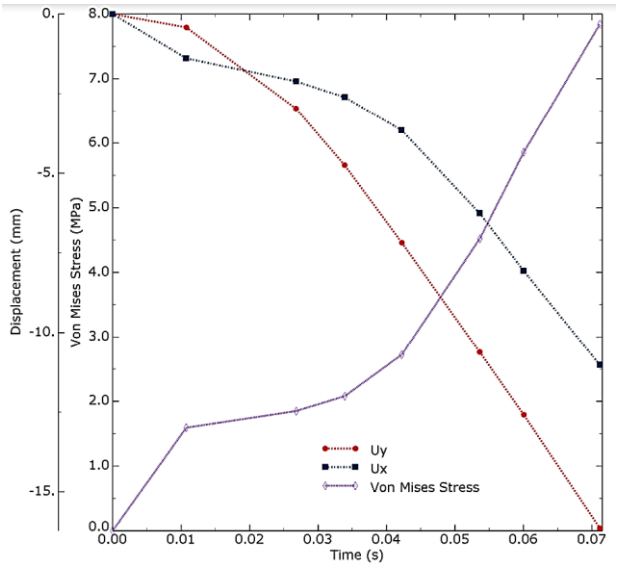

Figure 25: dependence of U_x, U_y and σ_{VM} versus time at point B

For prediction purposes, it is better to plot U_y as a function of U_x on one side and σ_{VM} as a function of both U_x and U_y on the other side (see Fig. 26).

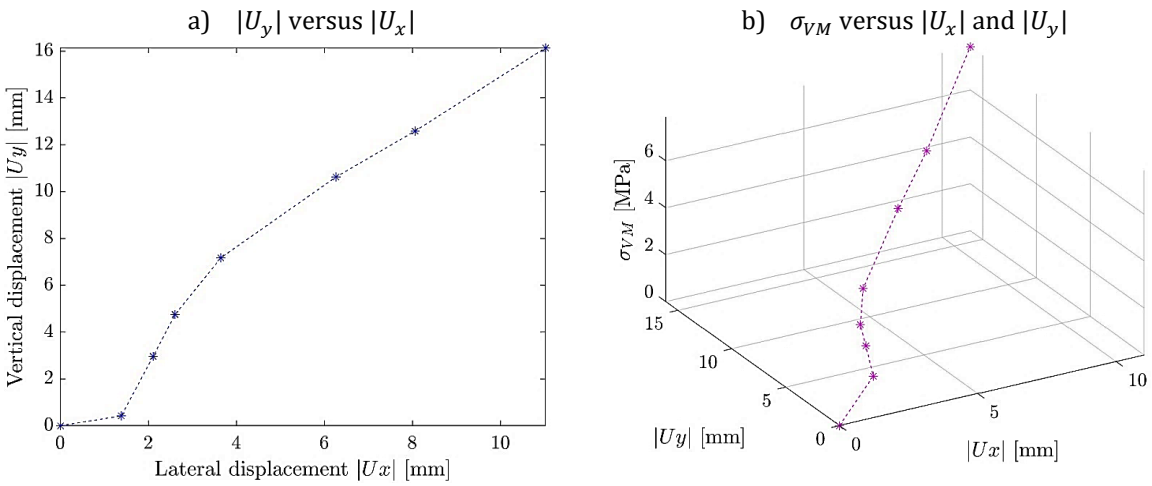

Figure 26: a) dependence of $|U_y|$ versus $|U_x|$. b) σ_{VM} versus $|U_x|$ and $|U_y|$ at point B

After the 4th converged step times, we notice that both curves evolve almost linearly. So, we can validate a linear tendency to make predictions for larger time ranges and resulting values of U_x, U_y and σ_{VM}. Similarly, we observe in Fig. 26 that there is a linear dependency between the variables beyond the first point. Therefore, we can use a linear approximation to predict any value of the displacements (U_x, U_y) and σ_{VM}.

Note: U_z at B is equal to zero at all time steps. Thus, we omitted it in the discussion.

4. Conclusion:

In a nutshell, the study presented in this paper provides a comprehensive approach to modeling and simulating the performance of rubber car tires using the finite element method. The research highlights the importance of optimizing tire design to enhance sustainability, given that a significant portion (about 30%) of oil consumption is attributed to rolling resistance. Through detailed simulations, complex scenarios such as steady state, layer delamination, inflation, and structural failure can be studied more deeply since the proposed model accurately reflects tires' real structure and mechanical properties.

The results demonstrate that the proposed simulation strategy can effectively predict the behavior of tires under different conditions, enabling the construction of tires with precisely defined strength and performance characteristics. This capability is crucial for improving modern tire design and ensuring durability, safety, and efficiency. Moreover, the study's findings indicate that a linear approximation can be used to predict displacements and stress values over larger time ranges, which is valuable for long-term performance assessments.

Future works will expand on this foundation by incorporating the effects of rubber hyperelasticity and viscoelasticity, providing an even more robust and realistic simulation framework. This ongoing research promises to further enhance the accuracy and reliability of tire performance predictions, contributing to the development of more sustainable and efficient tire technologies.

Acknowledgements:

The authors acknowledge the funding provided by the University of Pardubice through the grant number SGS 2024. This research work has been supported by the University of Pardubice grant number SGS 2024 and the Cultural and Educational Grant Agency of the Slovak Republic (KEGA), project No. KEGA 003TnUAD-4/2022 "Simulation of basic and specific experiments of polymers and composites based on experimental data in order to create a virtual computational-experimental laboratory of mechanical tests".

References

[1] R. A. Ridha, "Analysis for Tire Mold Design," *Tire Sci. Technol.*, vol. 2, no. 3, pp. 195–210, Aug. 1974, doi: 10.2346/1.2167186.
[2] C. F. Zorowski, "Mathematical Prediction of Dynamic Tire Behavior," *Tire Sci. Technol.*, vol. 1, no. 1, pp. 99–117, Feb. 1973, doi: 10.2346/1.2167157.
[3] A. Noor, "Nonlinear Analysis and Modeling of Tires. Final report," Charlottesville, VA (United States), 1996. [Online]. Available: https://www.osti.gov/biblio/382988
[4] P. A. Davis, "Comparison of 30X11.5 - 14.5 Bias-ply and Radial-belted Tire Characteristics," Oct. 1992. doi: 10.4271/922012.
[5] J. Krmela1, L. Beneš, and V. Krmelová, "Statical Experiments of Tire As Complex Long-Fibre Composite for Obtaining Material Parameters and Deformation Characteristics," *Mater. Eng.*, vol. 19, no. 3, pp. 124–135, 2012.
[6] Z. Li, Z. R. Li, and Y. M. Xia, "An Implicit to Explicit FEA Solving of Tire F&M with Detailed Tread Blocks," *Tire Sci. Technol.*, vol. 40, no. 2, pp. 83–107, Apr. 2012, doi: 10.2346/1945-5852-40.2.83.
[7] H. Wang, I. L. Al-Qadi, and I. Stanciulescu, "Simulation of tyre–pavement interaction for predicting contact stresses at static and various rolling conditions," *Int. J. Pavement Eng.*, vol. 13, no. 4, pp. 310–321, Aug. 2012, doi: 10.1080/10298436.2011.565767.
[8] W. Wang, S. Yan, and S. Zhao, "Experimental verification and finite element modeling of radial truck tire under static loading," *J. Reinf. Plast. Compos.*, vol. 32, no. 7, pp. 490–498, Apr. 2013, doi: 10.1177/0731684412474998.
[9] K. Drozd, S. Tarkowski, J. Caban, A. Nieoczym, J. Vrábel, and Z. Krzysiak, "Analysis of Truck Tractor Tire Damage in the Context of the Study of Road Accident Causes," *Appl. Sci.*, vol. 12, no. 23, p. 12333, Dec. 2022, doi: 10.3390/app122312333.
[10] LC Tyres, "Earthmover Tyre Damage Information Booklet," 22 Ballymount Rd Dublin. [Online]. Available: http://lctyres.ie/cars/
[11] Dassault Systemes Simulia Corpia Corp, "ABAQUS/Standard User's Manual, Version 6.9," *Dassault Syst. Simulia Corpia Corp*, 2020.
[12] Y. Li, X. Sun, J. Song, S. Zhang, and S. Han, "Topological structure and experimental investigation of a novel whole tire bead," *Mater. Des.*, vol. 203, p. 109592, 2021, doi: 10.1016/j.matdes.2021.109592.
[13] tire works total car cares, "Tire Terminology." https://tireworks.net/resources/tire-terminology/ (accessed Jul. 05, 2023).
[14] P. Farah, W. A. Wall, and A. Popp, "A mortar finite element approach for point , line , and surface contact," no. September 2017, pp. 255–291, 2018, doi: 10.1002/nme.5743.
[15] A. Popp, "Mortar Methods for Computational Contact Mechanics and General Interface Problems," no. September, 2012.
[16] G. Wang, W. Wang, C. Liang, and L. Cao, "Fatigue life prediction of radial tire bead using a maximum strain energy density range method," *Appl. Sci.*, vol. 11, no. 12, 2021, doi: 10.3390/app11125477.
[17] R. J. Boulbes, *Troubleshooting Finite-Element Modeling with Abaqus*. Cham: Springer International Publishing, 2020. doi: 10.1007/978-3-030-26740-7.